Nanostar Self-Assemblies of Spherical Nanoparticles Inside Lipid Vesicles

Soft Matter

ARTICLE TYPE

Nanostar Self-Assemblies of Spherical Nanoparticles inside Lipid Vesicles[†]

Yu Zhu,[a,b] Abash Sharma,[a,c] Eric J. Spangler,[a] and Mohamed Laradji[a*]

Curvature deformations of lipid membranes resulting from the adhesion of nanoparticles (NPs) often lead to effective interactions between the NPs, resulting in their self-assembly. Many studies have shown that this interaction is attractive in the case of NPs with uniform surfaces adhering to the outer leaflet of lipid vesicles. This interaction leads to the NPs' self-assembly into in-plane or out-of-plane linear chains in which they are unidimensionally close-packed. In this article, we show, through coarse-grained molecular dynamics simulations, that spherical NPs with uniform surfaces adhering to the inner leaflet of lipid vesicles experience repulsive interactions, resulting in NPs configurations in which they are apart. Systematic simulation sets with respect to the number of NPs inside vesicles and the strength of their adhesion to the membrane show an interesting phase diagram with different adhesion modes. These include a three-dimensional clustering mode, which is fairly dynamic at low adhesion strength and rigid at moderately high adhesion strength. These two regimes are separated by an intriguing two-dimensional clustering mode at moderate values of the adhesion strength. In this mode, the NPs form ordered planar nanostars with geometries determined by the number of NPs. In contrast to the three-dimensional mode, in the two-dimensional clustering mode, the NPs are anisotropically wrapped by the NPs with the largest degree of wrapping along the plane normal to the nanostar plane and the lowest degree of wrapping along the plane of the nanostar.

1 Introduction

There are numerous instances where micro- or nanosized particles embedded in a soft material experience effective interactions that are mediated by the embedding material. For example, non-adsorbing colloidal particles in a solution of smaller particles deplete the smaller particles from the vicinity of the colloidal particles. This results in an effective, entropy-driven attractive force between the colloidal particles called the depletion interaction.[1] Nanoparticles (NPs) in a microphase-separated diblock copolymer melt experience an effective, attractive force resulting from the stretching and compression of the polymers near the interface between the two blocks.[2,3] NPs in a polymer brush in a good solvent condition experience an entropically-driven attractive in-

teraction at strong enough NP-polymer interactions.[4] Nanosized particles, such as transmembrane proteins, that are embedded in lipid membranes can experience an attractive interaction driven by a mismatch between their hydrophobic thickness and that of the membranes.[5] Likewise, adhering NPs to lipid membranes can experience interactions resulting from curvature deformations of the membrane.[6–8]

The effective interactions between NPs, caused by an embedding agent, often lead to their self-assembly into ordered nanoclusters or nanocrystals.[9] The unique structural and functional properties displayed by nanoassemblies allow them to be potentially used in a range of advanced applications, including data storage[10], light harvesting,[11] non-linear optics,[12] catalysis,[13] and biosensing.[14] As a result, there has been a growing interest in using soft materials, such as copolymers,[15] DNA,[16,17] proteins,[18,19] cellulose,[20] and lipids,[21,22] as a self-assembly mediating agent in bottom-up nanofabrication.

The ability of lipid membranes, in particular, to induce interactions between adhering particles is due to their fluidity and flexibility. Hence, the adhesion of an NP to a lipid membrane, due to attractive forces between the NP's surface and the lipid head groups, leads to the wrapping of the NP by the membrane to a degree that depends on the competition between the adhesive inter-

a Department of Physics and Materials Science, The University of Memphis, Memphis, TN 38152, USA

b Borch Department of Medicinal Chemistry and Molecular Pharmacology, Purdue University, Lafayette, IN 47907, USA

c Department of Bioinformatics, University of Texas Southwestern Medical Center, Dallas, TX 75390, USA

* mlaradji@memphis.edu

action and the membrane's elastic energy.[23,24] The membrane's curvature deformations caused by the NP typically extend over length scales exceeding the NP's dimensions. Overlap between membrane curvature deformations caused by multiple adhering NPs leads to an effective interaction between the NPs.[7,8]

Most studies of NPs interacting with lipid membranes have been performed in the case where the NPs adhere to planar lipid membranes or the outer leaflet of lipid vesicles.[7,8,21,22,25–36] Free energy calculations of the arrangement of two NPs on the outer leaflet of a lipid vesicle show two states corresponding to the dimeric state, in which the NPs form an in-plane or an out-of-plane dimer or a monomeric state in which the NPs are apart.[7,8] The monomeric state dominates at low adhesive strength. In this case, the NPs are highly diffusive on the membrane due to the low amount of contact between the NPs and the lipids, and as a result, they can intermittently dimerize. At moderate values of the adhesive strength, the free energy exhibits two local minima corresponding to the monomeric and dimeric states, with the dimeric state becoming more stable than the monomeric state as the adhesion strength is increased.[8] This results in the aggregation of NPs into in-plane or out-of-plane chains at moderate values of the adhesive strength.[27,30]

Despite a wealth of studies on the spatial arrangement of NPs adhering to the outer leaflet of lipid vesicles, only a few investigations have been performed on the adhesion of NPs on the inner leaflet of lipid vesicles.[28,29,37–39] Most of these studies dealt with the adhesion of a single NP to the inner side of lipid vesicles. For example, Bahrami *et al.* showed that the wrapping process of an NP adhering to the outer side of a vesicle experiences an energy barrier that decreases with increasing vesicle's size.[38,40] In contrast, no energy barriers occur when the NPs adhere to the inner leaflet of lipid vesicles.[38] The earlier study by Saric and Cacciuto[28] on the aggregation of spherical NPs inside lipid vesicles was focused on the case where the size of the vesicle is much larger than that of the NPs. In the present study, we investigate the modes of adhesion of several spherical NPs with uniform surfaces inside relatively small lipid vesicles through molecular dynamics simulations. We focus, in particular, on the effect of the strength of the adhesive interaction and the number of NPs on the specific arrangement of the NPs. The salient results of this study are that NPs adhering to the inner leaflet of a vesicle experience an effective repulsive interaction and that for intermediate values of the adhesive interaction, the NPs self-assemble into quasi-two-dimensional star-like nanoclusters, in which the NPs are apart.

2 Model and Approach

The numerical simulations in the present study are based on a coarse-grained, implicit-solvent model in which a lipid molecule is coarse-grained into a short, semi-flexible chain composed of one head (h) bead and two tail (t) beads.[41,42] The interactions are tuned to allow the lipid chains to self-assemble into bilayer membranes with elastic constants that are in line with experimental values. Specifically, the potential energy of the bilayer is given by

$$U(\{\mathbf{r}_i\}) = \sum_{i,j} U_0^{\alpha_i \alpha_j}(r_{ij}) + \sum_{\langle i,j \rangle} U_{\text{bond}}^{\alpha_i \alpha_j}(r_{ij}) + \sum_{\langle i,j,k \rangle} U_{\text{bend}}^{\alpha_i \alpha_j \alpha_k}(\mathbf{r}_i, \mathbf{r}_j, \mathbf{r}_k), \quad (1)$$

where $\mathbf{r}_i$ is the coordinate of bead i, $r_{ij} = |\mathbf{r}_i - \mathbf{r}_j|$, and $\alpha_i (= h$ or t) is the type of bead i. $U_0^{\alpha_i \alpha_j}(r_{ij})$ in Eq. (1) is a pair potential between particles i and j, and for the sake of the computational efficiency of the model, this potential is chosen to be a soft pairwise function given by

$$U_0^{\alpha\beta}(r) = \begin{cases} \left(U_{\text{max}}^{\alpha\beta} - U_{\text{min}}^{\alpha\beta}\right) \frac{(r_m - r)^2}{r_m^2} + U_{\text{min}}^{\alpha\beta} & \text{if } r \leq r_m, \\ -2\, U_{\text{min}}^{\alpha\beta}\, \frac{(r_c - r)^3}{(r_c - r_m)^3} + 3\, U_{\text{min}}^{\alpha\beta}\, \frac{(r_c - r)^2}{(r_c - r_m)^2} & \text{if } r_m < r \leq r_c, \\ 0 & \text{if } r > r_c, \end{cases} \quad (2)$$

where $U_{\text{max}}^{\alpha\beta} > 0$ and $U_{\text{min}}^{\alpha\beta} \leq 0$. Due to the lack of explicit solvent in this model, self-assembly of bilayer membranes is achieved by choosing an attractive interaction between tail beads, i.e., $U_{\text{min}}^{tt} < 0$. Otherwise, the pair potential of other pairs of beads is fully repulsive, i.e., $U_{\text{min}}^{hh} = U_{\text{min}}^{ht} = 0$. To maintain continuity and smoothness of the two-body interaction in Eq. (2), the potential in the interval $r_m \leq r \leq r_c$ is chosen to be a third-order polynomial. Furthermore, despite the softness of the two-body interaction in Eq. (2), compared, for example, to the Lenard-Jones potential, it provides beads with an excluded volume, as shown by Fig. S1 (ESI†).

Connectivity between consecutive beads in a lipid chain is maintained by the second term in Eq. (1), which is given by

$$U_{\text{bond}}^{\alpha_i \alpha_j}(r_{ij}) = \frac{k_{\text{bond}}^{\alpha_i \alpha_j}}{2} \left(r_{ij} - a_{\alpha_i \alpha_j}\right)^2, \quad (3)$$

where $k_{\text{bond}}^{\alpha_i \alpha_j}$ is the bond stiffness coefficient and $a_{\alpha_i \alpha_j}$ is the preferred bond length between beads i and j. We note that bonded beads in a lipid chain interact as well via $U_0^{\alpha_i \alpha_j}$.

Finally, $U_{\text{bend}}^{\alpha\beta\gamma}$ in Eq. (1) is a three-body potential that provides bending stiffness to the lipid chains and is given by

$$U_{\text{bend}}^{\alpha_i \alpha_j \alpha_k}(\mathbf{r}_i, \mathbf{r}_j, \mathbf{r}_k) = \frac{k_{\text{bend}}^{\alpha_i \alpha_j \alpha_k}}{2} \left(\cos \varphi_0^{\alpha_i \alpha_j \alpha_k} - \frac{\mathbf{r}_{ij} \cdot \mathbf{r}_{kj}}{r_{ij} r_{kj}}\right)^2, \quad (4)$$

where $k_{\text{bend}}^{\alpha_i \alpha_j \alpha_k}$ is the bending stiffness coefficient of triplet (i, j, k), and $\varphi_0^{\alpha_i \alpha_j \alpha_k}$ is the preferred splay angle of the triplet. The bending modulus of a bare membrane, extracted from the spectrum of the height fluctuations, with the interaction parameters provided in Table 1, is $\kappa \approx 30 k_B T$,[42] which is comparable to that of a DPPC bilayer in the fluid phase.[43]

The NPs in this study are modeled using the same model we introduced earlier.[31,33–35,44,45] Namely, we begin with an icosahedron mesh, which is triangulated thrice, resulting in 642 nodes (beads of type n) and 1280 elementary triangles.[46] The nodes are subsequently projected onto a sphere of diameter D_{NP}, with the same center as the original icosahedron. Two neighboring beads of the NP are connected via the harmonic potential given by Eq. (3) with a bond stiffness k_{bond}^{nn} and a bond length a_{nn}. Every triplet of connected beads of the NP experiences the three-body interaction given by Eq. 4 with a bending stiffness k_{bend}^{nnn} and a pre-

Table 1 Model parameters. In this table ε is an energy scale related to temperature ($\varepsilon = k_B T / 3$). The minimum of the potential energy between an n bead and a lipid head bead, i.e., $\mathscr{E}$, is a multiple of ε and is varied in the simulations. $r_m = 1$ nm and $D_{NP} = 20$ nm.

Parameter	Value
$U_{\max}^{hh}$, $U_{\max}^{ht}$	100ε
$U_{\max}^{tt}$	200ε
$U_{\min}^{hh}$, $U_{\min}^{ht}$	0
$U_{\min}^{tt}$	-6ε
$U_{\max}^{nh}$	200ε
$U_{\min}^{nh}$	$-\mathscr{E}$
$U_{\max}^{nt}$	100ε
$U_{\min}^{nt}$	0
$U_{\max}^{nn}$	200ε
$U_{\min}^{nn}$	0
k_{bond}^{ht}, k_{bond}^{tt}	$100\varepsilon / r_m^2$
k_{bend}^{htt}	100ε
k_{bond}^{nn}	1200ε
k_{bond}^{nn}	$1200\varepsilon / r_m^2$
k_{bond}^{nc}	$45\varepsilon / r_m^2$
k_{bend}^{nnn}	250ε
r_c	$2r_m$
a_{ht}, a_{tt}	$0.7r_m$
a_{cn}	$D_{NP}/2$

ferred bond angle φ_0^{nnn} determined by the initial configuration of the NP. We found that since the NP is hollow, this three-body interaction is not enough to maintain an almost spherical geometry for the NPs. This problem is circumvented by inserting a bead of type c at the center of the NP, which is bonded to all n-beads of the NP's surface by a harmonic potential given by Eq. (3) with a bond stiffness k_{bond}^{cn} and a preferred bond length $a_{cn} = D_{NP}/2$, where D_{NP} is the NP's diameter. Fig. S2 (ESI†) depicts a snapshot of an NP at equilibrium.

The n-beads comprising an NP interact with the lipid beads through the potential given by Eq. (2). To promote the adhesion of the NP to the membrane, the n-beads of the NP interact attractively with the lipid h-beads, i.e., $U_{\min}^{nh} < 0$ However, the interaction between the n and t-beads is repulsive, i.e., $U_{\min}^{nt} = 0$. We consider the case where the NPs interact repulsively with each other, i.e., $U_{\min}^{nn} = 0$, to prevent their aggregation in the absence of lipid membranes.

Table 1 gives the values of the model parameters. With these parameters, lipid chains spontaneously self-assemble into bilayer membranes. The bending modulus of the bilayer, as extracted from the spectrum of its height fluctuations, is $\kappa \approx 30 k_B T$ [42] in the case where $\varepsilon = k_B T / 3$, where k_B is Boltzmann's constant and T is temperature. This value of the bending modulus is in line with that of a DPPC bilayer in the fluid phase [43].

All beads are moved using a molecular dynamics scheme with

a Langevin thermostat [47],

$$\dot{\mathbf{r}}_i(t) = \mathbf{v}_i(t)$$

$$m\dot{\mathbf{v}}_i(t) = -\nabla_i U(\{\mathbf{r}_i\}) - \Gamma \mathbf{v}_i(t) + \sigma \chi_i(t), \qquad (5)$$

where m is the mass of a bead (same for all beads), Γ is a bead's friction coefficient, and $\sigma \chi_i(t)$ is a random force originating from the heat bath. $\chi_i(t)$ is a random vector generated from a uniform distribution [48,49] and obeys $\langle \chi_i(t) \rangle = 0$ and $\langle \chi_i^{(\mu)}(t) \chi_j^{(\nu)}(t') \rangle = \delta_{\mu\nu} \delta_{ij} \delta(t - t')$, where μ and ν are x, y or z. Numerically, $\chi_i^{(\mu)} \in [-\sqrt{3/\Delta t}, \sqrt{3/\Delta t}]$, where Δt is the integration time step. The dissipative and random forces are related to each other by the dissipation-fluctuation theorem, which leads to $\Gamma = \sigma^2 / 2k_B T$. The equations of motion are integrated using the velocity-Verlet approach [50] with $\Gamma = \sqrt{6}m/\tau$ and a time step $\Delta t = 0.02\tau$.

From the simulations, the thickness of the lipid bilayer in the fluid phase is found to be about $4r_m$. The typical thickness of a phospholipid bilayer in the fluid phase is about 4 nm. We therefore estimate $r_m \approx 1$ nm. All lengths are, therefore, expressed in nanometers. The strength of the interaction between an NP and the membrane is expressed in terms of the adhesion energy density, defined as $\xi = |U_{adh}|/A_{adh}$, where U_{adh} is the net potential energy between the NP and the membrane and A_{adh} is the area of the NP adhering to the membrane. ξ is directly related to the strength of the interaction between n- and h-beads. ξ vs $\mathscr{E}$ in the case of a 20-nm NP is shown in Fig. S3 (ESI†).

Simulations are performed on lipid vesicles without volume constraint. This corresponds to the case where the vesicles are prepared experimentally in an isotonic condition or pure water without added buffer or solutes. The slow transport of water through lipid membranes can be overcome by the incorporation of transmembrane aquaporin channels within the membrane of the vesicle. [51,52] Aquaporin passively translocates water molecules, thus allowing the vesicle to adjust its volume freely. In the simulations, the diameter D_{LV} of the vesicle is varied between 52.6 and 96 nm. Here, D_{LV} is defined as twice the average distance between the positions of the h-beads of the outer leaflet and the center of mass of the vesicle. This range of D_{LV} corresponds to a total number of lipid chains in a vesicle ranging between 30 000 and 100 000). The diameter of the NPs is $D_{NP} = 20$ nm. In a typical simulation, n NPs are initially placed inside an equilibrated vesicle at random positions such that they are not in contact with the membrane.

3　Results and Discussions

Earlier numerical studies of two NPs adhering to the outer side of vesicles show two arrangement modes corresponding to the dimeric state, in which the NPs are in contact and form either an in-plane or an out-of-plane dimer, and the monomeric state, in which the NPs are apart. [7,8] To determine the preferred arrangement of two NPs adhering to the inner side of a vesicle, we performed several sets of umbrella sampling simulations [53] with the following bias harmonic potential energy between the center c-
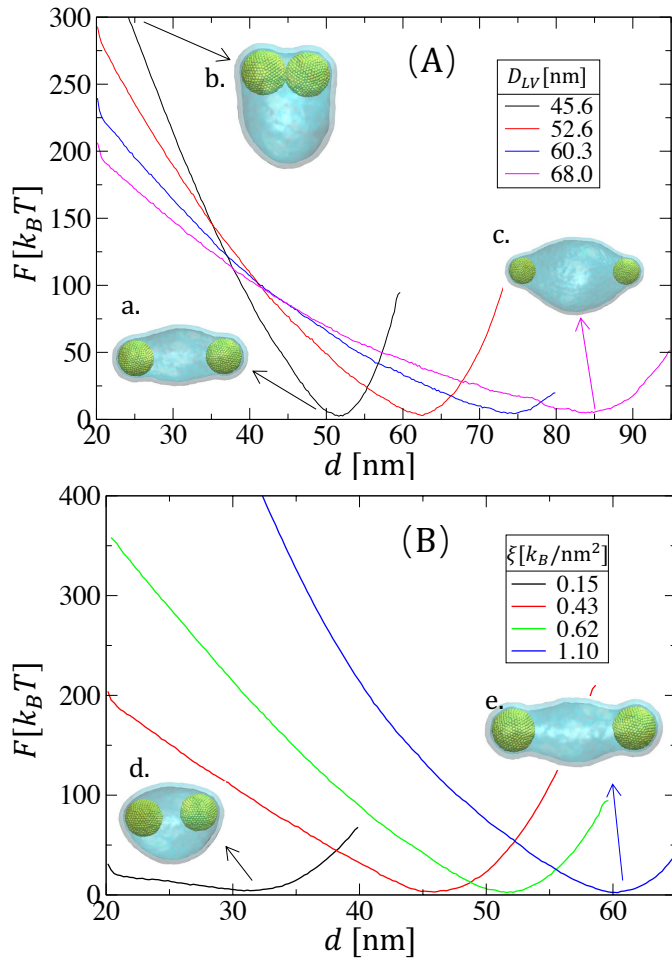
Fig. 1 (A) Free energy as the function of the distance between two NPs' centers for different values of the diameter of lipid vesicles, at $\xi = 0.62\,k_BT/\mathrm{nm}^2$. (B) Free energy as a function of the distance between two NPs' centers for different values of adhesion strength between NPs and lipid vesicles, at $D_{LV} = 45.6\,\mathrm{nm}$. Snapshots (a-e) are obtained from wham simulations with different biased distances between NPs.
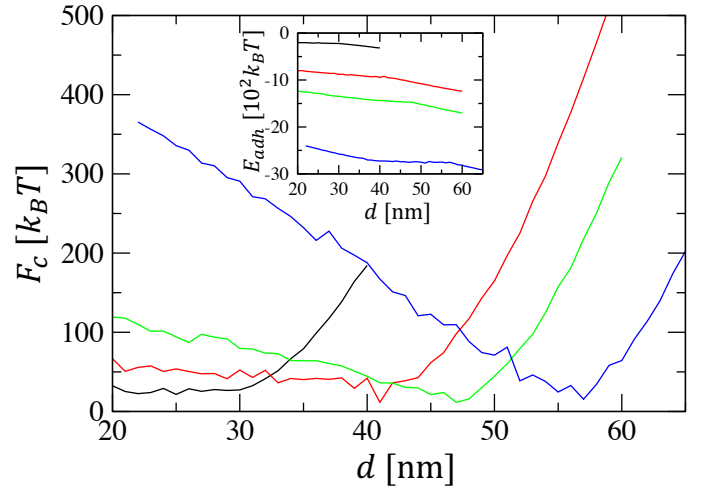

Fig. 2 Curvature free energy as the function of the distance between the two NPs, d, for the systems shown in Fig. 1 (B). Curves were translated such that their minima have almost the same value. The curves' colors correspond to the legends in Fig. 1 (B) (Inset) Adhesion energy versus d for the systems shown in the main figure.

beads of the two NPs,

$$U_{\mathrm{bias}} = \frac{k_{\mathrm{bias}}}{2}(d - d_{\mathrm{bias}})^2, \qquad (6)$$

where $k_{\mathrm{bias}} = 100\varepsilon/\mathrm{nm}^2$, d is the reaction coordinate, and d_{bias} is varied between $21\,\mathrm{nm}$ and a maximum value that depends on the size of the vesicle and ξ. To ensure overlap between consecutive histograms of d, we use a step in d_{bias} equal to $0.5\,\mathrm{nm}$. The histograms generated from these simulations are then combined using the weighted histogram analysis method (WHAM) to calculate the free energy as a function of d.[54]

The free energy obtained from these calculations, shown in Fig. 1(A) for a moderate value of the adhesive strength corresponding to $\xi = 0.62\,k_BT/\mathrm{nm}^2$, exhibits a single minimum. This corresponds to an arrangement of the NPs in which they are far from each other, regardless of the size of the vesicle. Moreover, the preferred distance between the NPs increases with D_{LV}. These results are validated by unbiased simulations starting with two NPs that are close to each other, which shows that the preferred

equilibrium distance between the NPs for different vesicle sizes, depicted in Fig. S4, agrees with the location of the free energy minimum in Fig. 1(A). Furthermore, Fig. 1(B) shows that for a given vesicle size, the location of the free energy minimum increases with increasing ξ. Fig. 1 therefore indicates that the vesicle induces an effective repulsive interaction between NPs.

The behavior of NPs adhering to the inner side of a vesicle is fundamentally different from that of two NPs adhering to the outer side of a vesicle. In the latter case, the free energy exhibits two local minima, corresponding to a dimeric state at low d values and a monomeric state at high d values. The absence of the dimeric state in the case of NPs adhering to the inner side of the vesicle is inferred from the net adhesion potential energy of the NPs to the vesicle U_{adh} and the curvature free energy $F_c = F - U_{adh}$ shown as a function of d in Fig. 2 for the case of $D_{LV} = 45.6$ nm. This figure demonstrates that both $U_{adh}(d)$ and $F_c(d)$ decrease monotonically with d for low values of d, regardless of the value of ξ. This prevents the free energy from exhibiting a local minimum at low values of d. In contrast, Fig. 2 shows that $U_{adh}(d)$ also decreases with d while $F_c(d)$ increases with d at high values of d, leading to a local minimum in the free energy corresponding to the monomeric state. This behavior is different from the case of NPs adhering to the outer side of vesicles, in which the dependence of the adhesion potential on d is not monotonic.[8]

We now focus on the preferred spatial arrangement of more than two NPs inside lipid vesicles. Toward this goal, we first performed a large number of unbiased molecular dynamics simulations of n NPs, with $3 \leq n \leq 10$, at values of the adhesion strength $0.25\,k_BT/\mathrm{nm}^2 < \xi < 2.8\,k_BT/\mathrm{nm}^2$. These energy densities are in line with those of NPs coated with neutravidin proteins adhering to a membrane with biotinylated lipids,[55] or those of Au NPs with charged ligands adhering to phospholipid membranes.[56] In our simulations, the ratio between the vesicle area and the net area of the NPs, $\rho = D_{LV}^2/nD_{NP}^2 = 2.31$. This corresponds to vesicles with
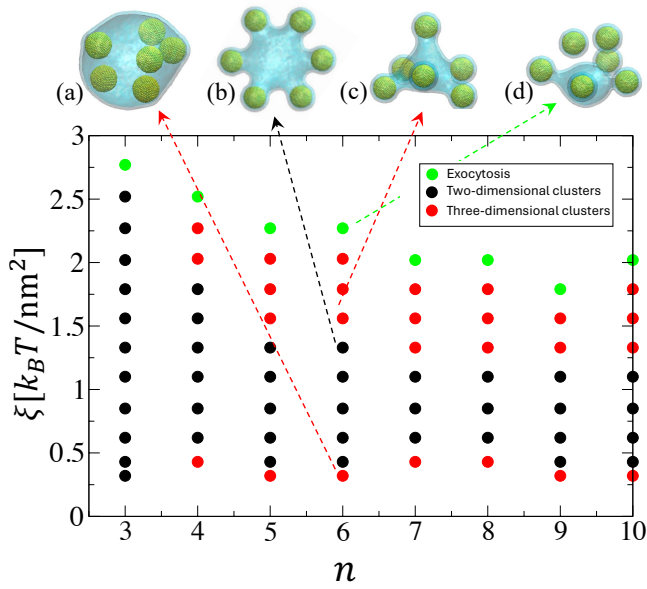
Fig. 3 Adhesion modes phase diagram of spherical NPs inside a vesicle in terms of the number n of the NPs and adhesion strength ξ. This phase diagram is determined in the case of $\rho = 2.31$. Snapshots (a) to (c) correspond respectively to configurations in the three-dimensional clustering mode at low ξ, the two-dimensional clustering mode at intermediate ξ, the three-dimensional clustering mode at relatively high ξ, and the exocytosis mode at high ξ in the case of $n = 6$.

52.6 nm $< D_{LV} \leq 96.2$ nm. The obtained phase diagram of the NPs' adhesion modes, depicted in Fig. 3, shows three main adhesion modes, corresponding to a three-dimensional clustering mode of the NPs (red points in Fig. 3), a surprising two-dimensional clustering mode at intermediate values of ξ (black points in Fig. 3), and (3) an exocytosis mode at high values of ξ (green points in Fig. 3). In the interesting two-dimensional clustering mode at intermediate ξ, the NPs form nicely ordered nanostars, as demonstrated by the equilibrium snapshots for different values of n in Fig. 4. The left row of these snapshots qualitatively demonstrates that these configurations are quasi-two-dimensional. The two-dimensional nature of these clusters will be quantified later.

The phase diagram exhibits an interesting reentrant phase behavior with respect to ξ, characterized by the presence of a three-dimensional clustering mode at low and relatively high values of ξ, sandwiching the two-dimensional clustering mode at intermediate values of ξ. At low values of ξ, the degree of wrapping of the NPs is weak (see snapshot (a) in Fig. 3). As a result, the three-dimensional clusters are very dynamic, as demonstrated by the large fluctuations in the distances between the NPs shown in Fig. S6(A) (ESI†). In contrast, NPs are strongly wrapped in the three-dimensional clustering mode at high ξ (see snapshot (c) in Fig. 3). This results in a much more rigid structure than at low ξ, as demonstrated by the weak time dependence of the distances between the NPs shown in Fig. S6(B) (ESI†). Both three-dimensional clusters at low and high values of ξ are disordered, as demonstrated by their broad radial distribution function (RDF) shown in Fig. 5 for the case of $n = 6$ at $\xi = 0.35 k_B T / \text{nm}^2$ and $1.56 k_B T / \text{nm}^2$. In contrast, the ordered two-
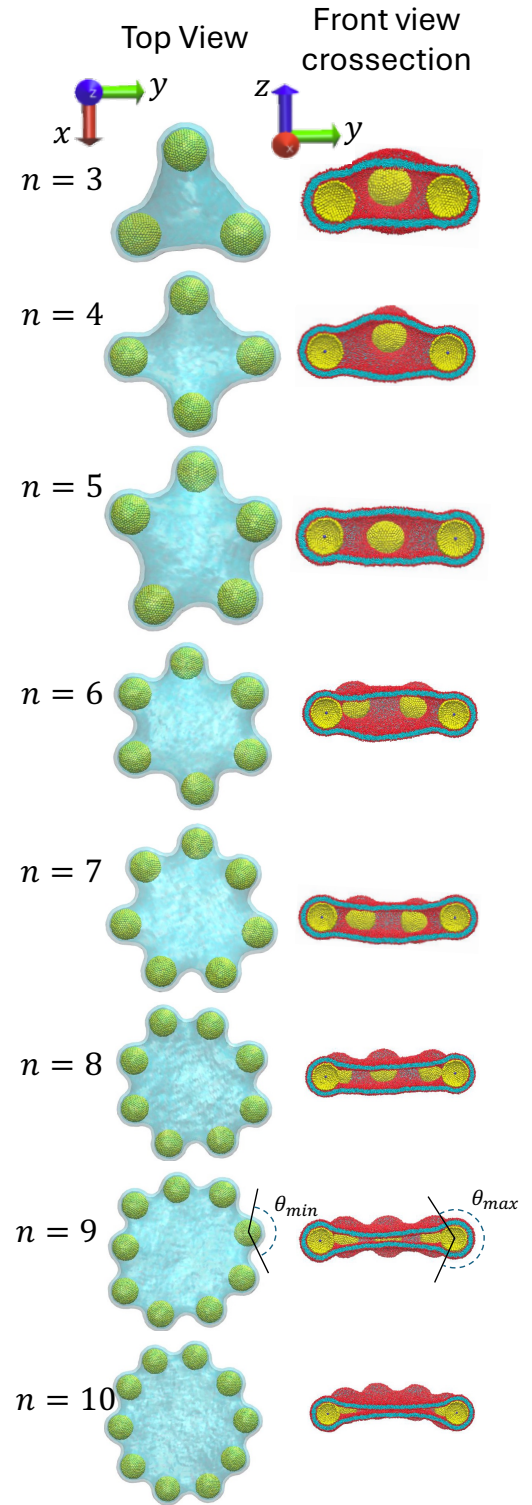

Fig. 4 Equilibrium configurations of n NPs adhering to the inner side of a vesicle at $\xi = 0.85 k_B T / \text{nm}^2$. Here, the ratio between the net area of the vesicle and the NPs, i.e., $\rho = D_{LV}^2 / n D_{NP}^2 = 2.31$. The NPs are yellow, the lipid tails are icy blue and the lipids heads are red. The lipid heads are not shown in the left column. The lateral degree of wrapping θ_{min} and transverse degree of wrapping θ_{max} demonstrate that in the case where the NPs form nanostars, their degree of wrapping is anisotropic.
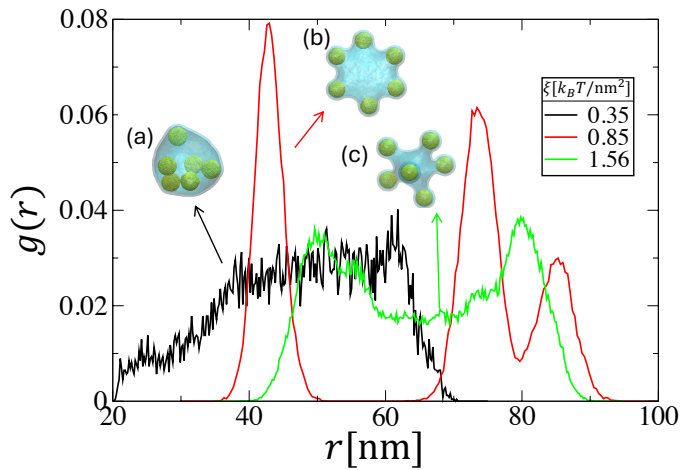
Fig. 5 Radial distribution function, $g(r)$, at three different values of ξ, for the case of $n = 6$. Also shown are equilibrium snapshots corresponding to the three values of ξ.

Fig. 6 (A) Coplanarity, λ, versus time for $3 \leq n \leq 10$ at $\xi = 0.85 k_B T/\text{nm}^2$ and $\rho = 2.31$. (B) A time series of snapshots demonstrating the evolution of the NPs arrangement from a three-dimensional nanocluster to a two-dimensional nanocluster during equilibration starting from a disordered placement of the NPs inside an equilibrated vesicle.

dimensional clusters exhibit well-defined peaks as shown by its RDF at $\xi = 0.85 k_B T/\text{nm}^2$ Fig. 5.

Figure 3 shows that the interesting two-dimensional clustering of NPs occurs over a wide range of adhesion strength. The series of snapshots for different values of n at $\xi = 0.85 k_B T/\text{nm}^2$, shown in Fig. 4, qualitatively demonstrates that NPs' nanoclusters are fairly ordered polyhedra with vertices occupied by the NPs. The two-dimensional character of these nanoclusters is quantified through the coplanarity of NPs, defined as

$$\lambda = \sqrt{f(A^*, B^*, C^*, D^*)}, \tag{7}$$

where

$$f(A, B, C, D) = \frac{1}{n} \sum_{i=1}^{n} \frac{(Ax_i + By_i + Cz_i + D)^2}{A^2 + B^2 + C^2}, \tag{8}$$

and A^*, B^*, C^*, and D^* are the values of A, B, C and D that minimize f, and (x_i, y_i, z_i) are the coordinates of the ith NP. Fig. 6(A), which depicts the time evolution λ at $\xi = 0.85 k_B T/\text{nm}^2$ and $\rho = 2.31$, shows that the coplanarity becomes very small (considerably smaller than the diameter of the NPs) at late times regardless of the number of NPs. The flattening of the NPs' cluster is shown qualitatively by Fig. 6(B) for the case of $n = 10$. This indicates that at equilibrium, the NPs form quasi-two-dimensional nanoclusters. Fig. 7, which depicts the coplanarity as a function of ξ in the case of $n = 6$, shows that λ depends nonmonotonically on ξ. The high values of λ at low ξ indicate that NPs form a three-dimensional structure at low ξ. In contrast, λ is small at intermediate values of ξ ($0.4 k_B T/\text{nm}^2 \lesssim \xi \lesssim 1.5 k_B T/\text{nm}^2$), indicating that the NPs are practically coplanar at these values of ξ, in accord with Fig. 3. At moderately high values of ξ, λ is high, indicating that the NPs form three-dimensional nanoclusters in this regime. These results agree with the molecular dynamics study of Reynwar et al. [6] which shows that caps or capsids (Janus NPs), which adhere strongly to planar membranes, produce invaginations in which they form disordered three-dimensional nanoclusters where the particles are also apart from each other. Our results
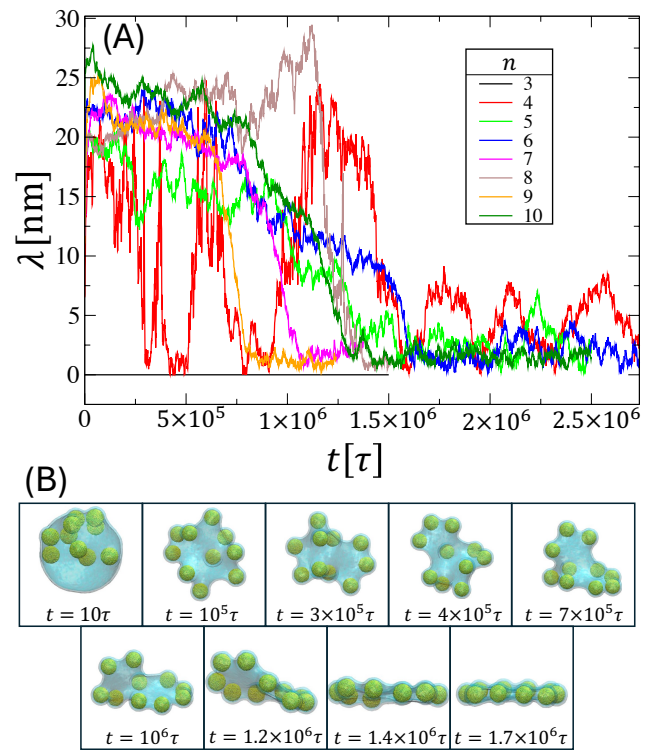
at moderately high values of ξ are also in qualitative agreement with the Monte Carlo simulations of triangulated surfaces by Atilgan and Sun, [57] in which they observed that conical inclusions with curvature having same sign as that of the embedding vesicle, tend to be dispersed randomly and remain apart.

The nanostar configurations shown in Fig. 4 are highly anisotropic. A qualitative inspection of the NPs' wrapping by the membrane, from Fig. 4, indicates that the degree of wrapping along the xy-plane is lower than that along the normal direction. This anisotropy in the degree of wrapping is qualitatively indicated by the wrapping angles θ_{min} and θ_{max} in Fig. 4 for the case of $n = 9$. To assess if this is indeed the case, we determined the instantaneous maximum and minimum wrapping angles of single NPs, i.e., θ_{max} and θ_{min}, of the NPs for low, intermediate, and high values of ξ, at which the NPs form three-dimensional, two-dimensional, and three-dimensional nanoclusters, respectively. Fig. 8 (A), (B), and (C) depict the instantaneous profile of the wrapping angles as a function of the azimuthal angle ϕ (defined in top right snapshot in Panel (D) of the figure) at $\xi = 0.35 k_B T/\text{nm}^2$, $0.85 k_B T/\text{nm}^2$, and $1.56 k_B T/\text{nm}^2$, respectively. These graphs show that the profiles are uniform (subject to fluctuations) at low and high values of ξ, at which the NPs clustering is three-dimensional. In contrast, the instantaneous profile is highly non-uniform in the case of $\xi = 0.85 k_B T/\text{nm}^2$, with azimuthal angles corresponding to consecutive minima and maxima separated by about 90°. Here, the minimum degree of wrapping
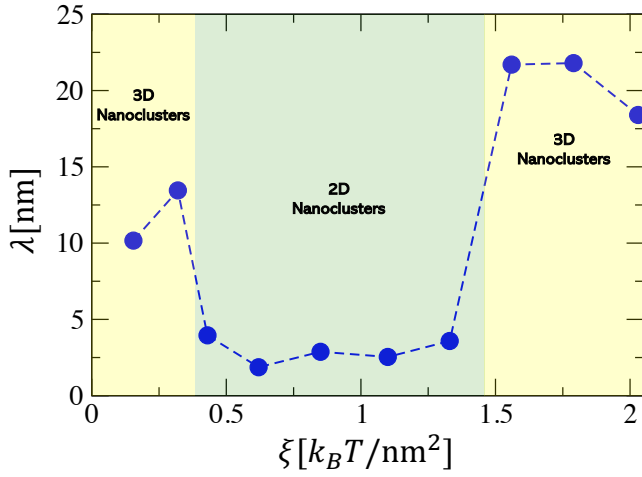
Fig. 7 Coplanarity, λ, versus adhesion strength ξ in the case of $n = 6$ at $\rho = 2.31$.

Fig. 8 (A-C) Profile of the wrapping angle θ as a function of the azimuthal angle ϕ for three different values of the adhesion strength corresponding to the case where the NPs form three-dimensional clusters (A,C) and two-dimensional clusters (B). (D) Snapshots of the lipid head groups that are in contact with the NP showing the maximum (left) and minimum (right) wrapping angles. (E) Time evolution of $\Delta\theta = \theta_{max} - \theta_{min}$ for the adhesion strengths shown in (A-C) Data shown in this figure correspond to the case of $n = 6$ and $\rho = 2.31$.

is along the plane that is parallel to that of the two-dimensional nanocluster and passing by the NP's center of mass. In contrast, the maximum degree of wrapping is along the plane perpendicular to the plane of the nanocluster and passing by the NP's center of mass. This indicates that the degree of wrapping is non-uniform in the case of two-dimensional clustering of the NPs. The time evolution of the difference between the instantaneous maximum and minimum degrees of wrapping, $\Delta\theta = \theta_{max} - \theta_{min}$ for all 6 NPs in the nanoclusters and for the three values of the adhesion strength is shown in Fig. 8 (E). This figure clearly demonstrates that when the NPs form two-dimensional nanoclusters (at $\xi = 0.85 k_B T / \text{nm}^2$), $\Delta\theta$ is substantially higher than when the NPs form three-dimensional nanoclusters, as a function of time for the three values of adhesion strength, is relatively small at low and high values of the adhesion strength. However, at $\xi = 0.85 k_B T / \text{nm}^2$, $\Delta\theta$ is clearly high in the case of quasi-two-dimensional clustering of the NPs.

Using the RDF, we now examine the degree of ordering of the NPs at intermediate values of ξ when they form quasi-two-dimensional nanoclusters. Fig. 9 depicts the RDFs of the NPs (based on their centers of mass) for values of $3 \leq n \leq 10$ in the case of $\xi = 0.85 \, \text{nm}^2 / k_B T$ and $\rho = 2.31$. This figure shows that $g(r)$ has a single peak in the case of $n = 3$, which implies that the NPs self-assemble into an equilateral triangle. In the cases of $n = 4$ and 5, $g(r)$ has two well-defined peaks, which is indicative of the fact that the NPs form a square and a regular pentagon, respectively. In the cases of $n = 6$ and 7, $g(r)$ exhibits three peaks, which indicates that the structures correspond to the regular hexagon and heptagon, respectively. Similarly, in the cases of $n = 8$ and 9, $g(r)$ exhibits four peaks, which indicates that the NPs are self-assembled into a regular octagon and nanogon, respectively. Finally, for $n = 10$, $g(r)$ exhibits four well-defined peaks, while a regular decagon should exhibit five peaks. We will show later that this is simply because the two last peaks are very close to each other and, due to fluctuations, effectively merge into a single peak.
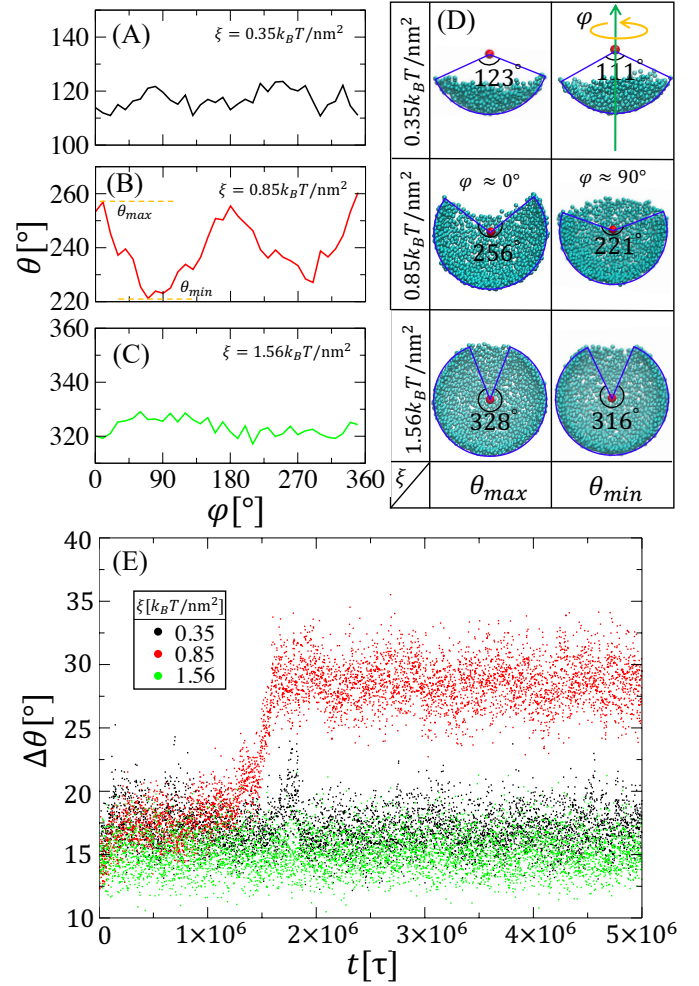
The quasi-two-dimensional nanoassemblies are further characterized by the ratios of the RDF peaks' positions in Fig. 9. These are obtained by fitting the RDF around the peaks with Gaussians and comparing the ratios r_i / r_1 with their corresponding ideal values, where r_i is the location of the RDF's peak i. The obtained values of r_i / r_1 for different values of n are shown in Table. S1 (ESI†). Also shown in this table are the values of r_i / r_1 in the case of regular polygons with n vertices. The values of r_i / r_1 are very close to those of the regular polygons, indicating that the quasi-two-dimensional nanoclusters at intermediate values of ξ are ordered.

The effect of vesicle size on the degree of order of the nanocluster was inferred by simulations in the case of $n = 6$ inside vesicles with D_{LV} ranging between 68 and 86 nm. We found that the hexagonal geometry of the nanocluster is preserved for all considered values of D_{LV}, as demonstrated by their correspond-
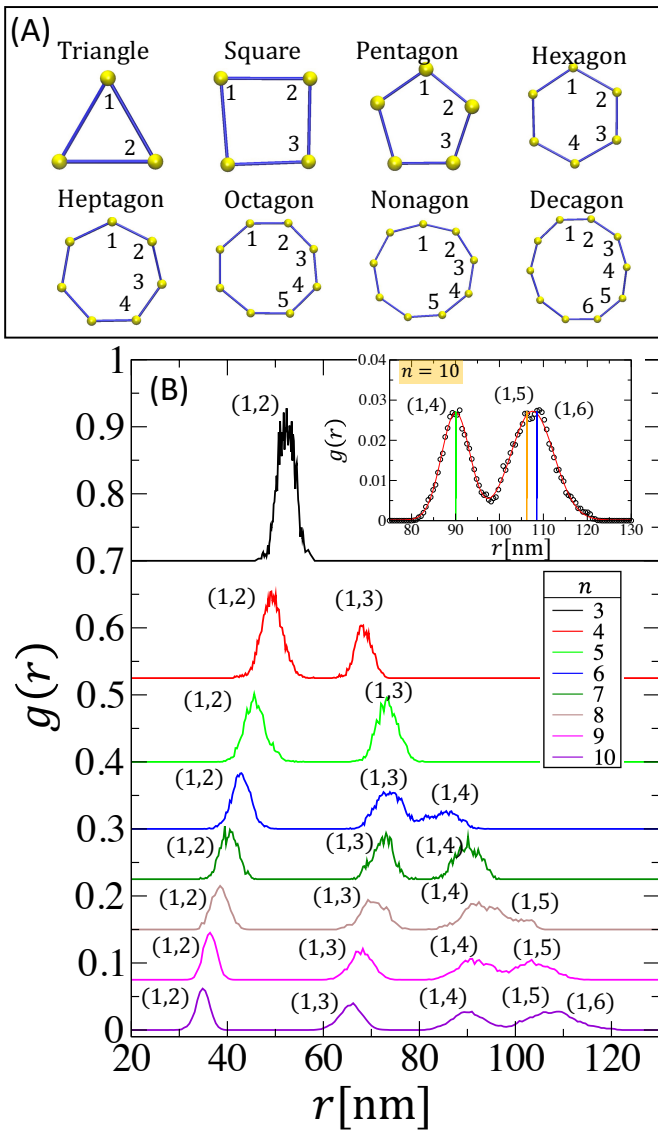
Fig. 9 (A) Geometries of the NPs' nanoclusters obtained from the simulations Vertices (yellow spheres) correspond to the NPs' centers. (B) Radial distribution function, $g(r)$, for different values of n, in the case of $\xi = 0.85\,\mathrm{nm}^2/k_BT$ and $\rho = 2.31$. The integers in the pairs next to the peaks correspond to the indices of the NPs in Panel (A). Inset of (B) shows the portion of the RDF in the case of $n = 10$ containing the three last peaks. The solid red line is a fit with the sum of three Gaussians. The locations of the peaks (1,4), (1,5), and (1,6) obtained from the fit are shown by the vertical green, orange, and blue lines, respectively.

ing RDFs in Fig. S5. However, the relative width $\Delta r_1/r_1$ of the first peak of the RDF, shown in the inset of Fig. S5, increases with D_{LV}, indicating an increase in the amount of fluctuations. We expect that the nanoclusters should become disordered beyond a certain vesicle size. However, from the inset of Fig. S5, this vesicle size should be quite large, and would require very large simulations.

We now address the interesting reentrant behavior of the three-dimensional clustering modes with increasing adhesion strength, as shown by Fig. 3. We recall that the results presented for each value of ξ are obtained from simulations starting from an equi-

librated vesicle with n NPs inside it but not adhering to its inner leaflet. These simulations yield configurations of the NPs at high ξ, which are localized spatially, as demonstrated by the distances between NPs versus time in Fig. S6 (ESI†). The inability of the nanoclusters to deform into two-dimensional clusters might be due to the presence of a high energy barrier between the two states. To infer if this is indeed the case, we performed upward and downward annealing simulations with respect to ξ, starting from a state where the NPs form a quasi-two-dimensional cluster and three-dimensional cluster, respectively. The details of the downward annealing simulation are as follows: Starting from an equilibrated configuration in the case of $n = 6$ and $\rho = 2.31$ at $\xi = 2.03k_BT/\mathrm{nm}^2$, the system is evolved for $3 \times 10^5\tau$ at $\xi = 1.79k_BT/\mathrm{nm}^2$. ξ is then suddenly reduced to $1.56k_BT/\mathrm{nm}^2$, at which the system is evolved for $3 \times 10^5\tau$. Finally, ξ is again suddenly reduced to $1.33_BT/\mathrm{nm}^2$, at which the system is evolved for $3 \times 10^5\tau$. The details of the upward annealing simulation are as follows: An equilibrated configuration in the case of $n = 6$ and $\rho = 2.31$ at $\xi = 1.33k_BT/\mathrm{nm}^2$ is evolved for $3 \times 10^5\tau$ at $\xi = 1.56k_BT/\mathrm{nm}^2$. ξ is then suddenly increased to $1.79k_BT/\mathrm{nm}^2$, at which the system is evolved for $3 \times 10^5\tau$. ξ is then suddenly increased again to $2.03_BT/\mathrm{nm}^2$, at which the system is evolved for $3 \times 10^5\tau$.

Fig. 10 shows the adhesion potential energy, the curvature energy, and the coplanarity as a function of time during the downward and upward annealing simulations described above. Here, the curvature energy is calculated using an approach based on the Helfrich Hamiltonian[58] in conjunction with a local Monge representation.[30] Fig. 10(C) shows that in the downward annealing simulation, the coplanarity remains high at $\xi = 1.79k_BT/\mathrm{nm}^2$ and $1.56k_BT/\mathrm{nm}^2$, implying that the nanocluster remains three-dimensional at these values of ξ. However, the coplanarity becomes very close to its value from the direct simulation at $\xi = 1.33k_BT/\mathrm{nm}^2$, which implies that the nanocluster becomes two-dimensional at this relatively low value of ξ. In contrast, in the upward annealing simulation, the coplanarity remains small at $\xi = 1.56k_BT/\mathrm{nm}^2$, $1.79k_BT/\mathrm{nm}^2$ and even at $2.03k_BT/\mathrm{nm}^2$, implying that the nanoclusters remain quasi-two-dimensional at these relatively high values of ξ, at which the direct simulations produce three-dimensional nanoclusters. These two-dimensional structures are either locally stable, which implies that an energy barrier must exist between the two-dimensional and three-dimensional states, or the nanoclusters are very slowly evolving into three-dimensional clusters. In the two-dimensional nanoclusters at moderate ξ, the degree of wrapping of the NPs is anisotropic, as discussed earlier (see Fig. 8(E)). In contrast, $\Delta\theta = \theta_{max} - \theta_{min}$ at $\xi = 2.03k_BT/\mathrm{nm}^2$ is independent of whether the nanoclusters are two- or three-dimensional, as demonstrated by Fig. S7. The two-dimensional nature of the nanoclusters during the upward annealing at high ξ could then be due to very slow kinetics.

4   Conclusion

This article reports results on the effective interaction and self-assembly of spherical NPs adhering to the inner leaflet of a lipid vesicle using molecular dynamics simulations of an implicit-
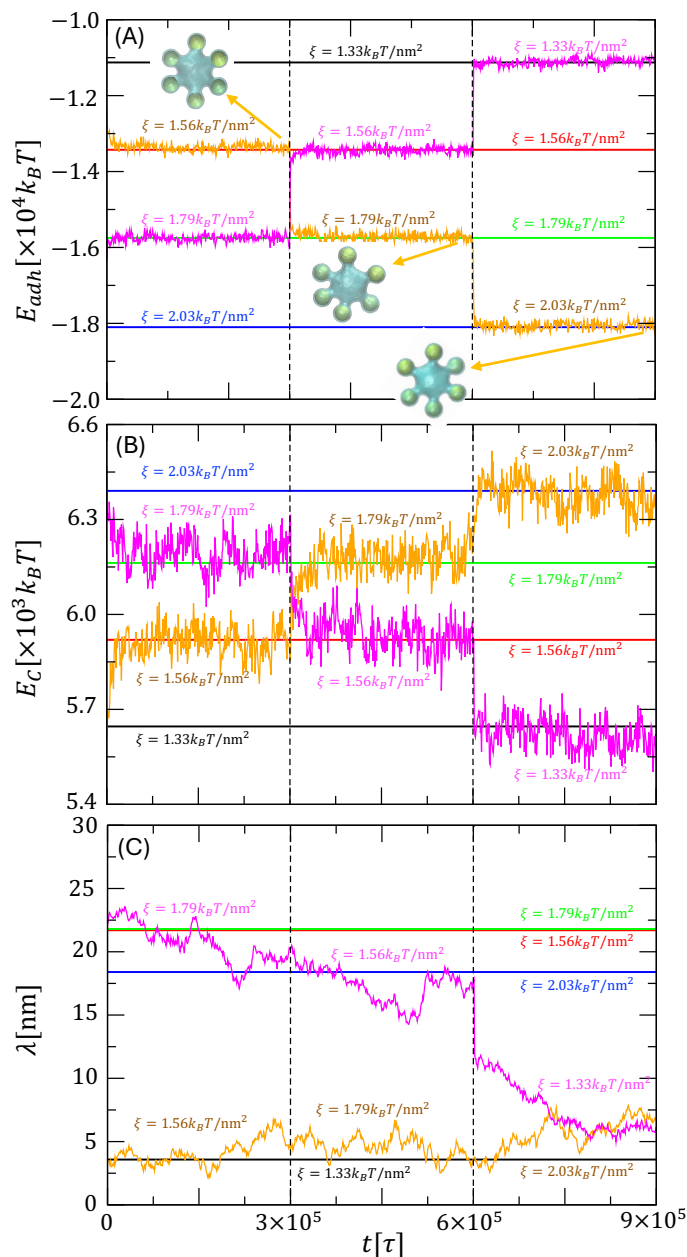
Fig. 10 Adhesion potential energy (A), curvature energy (B), and coplanarity (C) as a function of time during downward annealing simulation (magenta curves) and upward annealing simulation (orange curves). Details of these annealing simulations are found in the text Black, red, green, and blue solid lines indicate average values of the adhesion energy (in (A)), curvature energy (in (B)), and coplanarity (in (C)) Vertical dashed lines indicate the times at which ξ is suddenly changed All results in this figure are based on simulations of $n = 6$ with $\rho = 2.31$.

solvent model.[59] In this approach, the NPs are treated as hollow, relatively rigid triangulated meshes with spherical geometry and vertices occupied by beads. The results presented in this article are based on simulations of two NPs to determine the effective interaction between the NPs and simulations of three to 10 NPs to determine their preferred modes of adhesion as a function of the strength of the adhesive interaction.

Free energy calculations based on the weighted histogram anal-

ysis method[54] performed systematically as a function of adhesion strength and vesicle size show that two NPs inside a vesicle experience a repulsive interaction, regardless of the adhesion strength or diameter of the vesicle. This implies that NPs inside the vesicles cannot dimerize in contrast to NPs that adhere to the outer leaflet of lipid vesicles, which can experience both attractive and repulsive interactions.[7,8]

The central result of the present study is that several NPs adhering to the inner leaflet of a vesicle form intriguing, highly ordered two-dimensional nanostars in which the NPs are apart. The ordered nature of these nanoclusters is demonstrated by their radial distribution functions, and their two-dimensional character is demonstrated by the high coplanarity of the NPs' centers of mass. Interestingly, the membrane's wrapping of the NPs is anisotropic when they form a two-dimensional nanostar. The degree of wrapping of an NP is greatest along the plane perpendicular to the nanocluster's plane that passes by the NP's center of mass. However, the degree of wrapping is lowest along the plane parallel to the nanostar and passes by the NP's center of mass. We emphasize that the results above are obtained in the case where the vesicle can freely adjust its volume. This can be achieved, for example, by incorporating the transmembrane aquaporin channels within the membrane of the vesicle to facilitate passive transport of water molecules across the membrane.[51,52]. The cross-section of an aquaporin complex channel is about 8 nm^2,[60] which is substantially larger than the cross-section of a lipid molecule. As a result, the number of aquaporin complexes that can be incorporated in a single vesicle with a diameter about that in our simulations cannot be large without adversely affecting the bending rigidity of the membrane. In the presence of osmotically active particles that cannot cross the membrane, such as sugars or salts, the reduced volume $v = 6\pi^{1/2}V/A^{3/2}$, where $A_{LV} = \pi D_{LV}^2$ is the vesicle's area and V is the enclosed volume, can be decreased by tuning the concentration of the solute in the solution. This allows for low values of the reduced volume in the presence of NPs, leading to nanostar configurations similar to those in Fig. 4.

The phase diagram of the adhesion modes of several NPs inside a vesicle is characterized by a three-dimensional mode at low values of the adhesion strength in which the NPs are apart, weakly wrapped by the membrane, and highly diffusive. As the adhesion strength increases, the NPs form the two-dimensional nanostar assemblies discussed above. Interestingly, the phase diagram exhibits a reentrant behavior characterized by the reemergence of the three-dimensional clustering mode with increasing adhesion strength. However, in this structure, the NPs are spatially localized. Downward and upward annealing scans with respect to the adhesion strength show that the two-dimensional nanostars are preserved with increasing adhesion strength, which implies that there must exist a high-energy barrier between the two-dimensional and three-dimensional nanoclustering modes at moderately high adhesive strength. Experimentally, the different types of assemblies can be obtained by tuning the strength of the adhesive interaction between the NPs and the membrane. This can be achieved by tuning the grafting density of the ligands coating the NPs and by the concentration of the counterions in the solution.

In prior studies, we have shown that lipid vesicles can self-assemble Janus NPs, with spherical or spherocylindrical geometries adhering to the outer leaflet of lipid vesicles into highly ordered three-dimensional nanoclusters.[34,35] Janus NPs adhering to planar membranes also self-assemble into ordered hexagonal lattices.[45] The present study shows that lipid vesicles can also self-assemble NPs with uniform surfaces into two-dimensional ordered nanoclusters, provided that the NPs adhere to the inner side of lipid vesicles. This further demonstrates the potential of lipid membranes as an alternative bottom-up tool for fabricating nanostructures with specific geometries. Experimental validation of our results is warranted. We should note, however, that encapsulating NPs within vesicles is experimentally more challenging than allowing NPs to adhere to the outer surface of lipid vesicles through incubation, for example. As stated above, this difficulty is compounded with challenges in controlling small values of the volume-to-area ratio of the vesicles encapsulating the NPs. With these challenges, experimental validation of the results above in the near future experimentally is undoubtedly difficult. Experimental characterization of these nanostructures is also expected to be challenging due to their small size and may require tools such as cryogenic transmission electron microscopy. Although our simulations are performed on relatively small vesicles, the same results are expected in the context of larger NPs adhering to larger vesicles. Characterization of larger vesicles with larger NPs is less challenging than that of small vesicles with small NPs since it can be achieved through tools such as confocal microscopy. There have been many studies exploring the self-assembly of NPs mediated by various media. However, experimental studies of the self-assembly of NPs into ordered structures mediated by their adhesion to lipid membranes remain largely lacking. The unique highly-ordered two-dimensional nanoclusters observed in the present study should stimulate the exploration of lipid membranes as an effective tool for the self-assembly of nanomaterials.

Although the present study was conducted in the context of uniform spherical NPs, we also expect NPs with other geometries, adhering to the inner leaflet of lipid vesicles, to form ordered nanoclusters. For example, membrane-curvature-mediated interaction between spherocylindrical NPs adhering to the inner leaflet of lipid vesicles is also expected to be repulsive. A spherocylindrical NP adhering to a lipid membrane exhibits two modes corresponding to a parallel mode (where the principal axis of the NP is parallel to the membrane) at weak adhesive interactions and a normal mode (where the principal axis of NP perpendicular to membrane), at moderate adhesive interactions.[44] We therefore expect different types of nanoassemblies of spherocylindrical NPs adhering to the inner side a lipid vesicle. At relatively weak adhesive interactions, the spherocylindrical NPs may form two-dimensional polygonal nanoclusters, while at moderate adhesion strength, they may form star nanoclusters.

The present study was performed using a coarse-grained model, which accounts to some extent for the internal degrees of freedom of the lipid molecules and allows for lipids self-assembly into bilayer membranes. As such, the model is suitable for investigations of NPs with diameters comparable to the thickness of lipid membranes. The model simplifies molecular interactions and does not explicitly account for the ligands typically mediating the interaction between NPs and the lipid head groups. This simplification allows for large-scale simulations of vesicles with diameters close to 100nm encapsulating several 20-nm NPs. Although we expect the general results presented in this article to be independent of the details of the model, it would be, of course, desirable to validate our results using a more system-specific approach, such as the Martini model.[56]

Conflicts of interest

There are no conflicts of interest to declare.

Data availability

The data for this article, including a description of data types, are available at Open Science Framework at https://osf.io/xp8tj The molecular dynamics codes are available on GitHub at https://github.com/LaradjiSoftMatter/SoftMold.

Acknowledgements

Notes and references

1 H. N. W. Lekkerkerker, W. C.-K. Poon, P. N. Pusey, A. Stroobants and P. B. Warren, *Europhys. Lett.*, 1992, **20**, 559.

2 E. Reister and G. H. Fredrickson, *Macromolecules*, 2004, **37**, 4718–4730.

3 B. J. Lindsay, R. J. Composto and R. A. Riggleman, *J. Phys. Chem. B*, 2019, **123**, 9466–9480.

4 J. T. Mims, L. Tsuna, E. J. Spangler and M. Laradji, *J. Chem. Phys.*, 2024, **160**, 084906.

5 J. Killian, *Biochim. Biophys. Acta*, 1998, **1376**, 401–416.

6 B. J. Reynwar, G. Illya, V. A. Harmandaris, M. M. Müller, K. Kremer and M. Deserno, *Nature*, 2007, **447**, 461–464.

7 A. H. Bahrami, R. Lipowsky and T. R. Weikl, *Phys. Rev. Lett.*, 2012, **109**, 188102.

8 E. J. Spangler and M. Laradji, *J. Chem. Phys.*, 2021, **154**, 244902.

9 C. L. Bassani, G. van Anders, U. Banin, D. Baranov, Q. Chen, M. Dijkstra, M. S. Dimitriyev, E. Efrati, J. Faraudo, O. Gang, N. Gaston, R. Golestanian, G. I. Guerrero-Garcia, M. Gruenwald, A. Haji-Akbari, M. Ibáñez, M. Karg, T. Kraus, B. Lee, R. C. Van Lehn, R. J. Macfarlane, B. M. Mognetti, A. Nikoubashman, S. Osat, O. V. Prezhdo, G. M. Rotskoff, L. Saiz, A.-C. Shi, S. Skrabalak, I. I. Smalyukh, M. Tagliazucchi, D. V. Talapin, A. V. Tkachenko, S. Tretiak, D. Vaknin, A. Widmer-Cooper, G. C. L. Wong, X. Ye, S. Zhou, E. Rabani, M. Engel and A. Travesset, *ACS Nano*, 2024, **18**, 14791–14840.

10 S. Singamaneni, V. N. Bliznyuk, C. Binek and E. Y. Tsymbal, *J. Mater. Chem.*, 2011, **21**, 16819–16845.

11 S. Kundu and A. Patra, *Chem. Rev.*, 2017, **117**, 712–757.

12 J.-M. Lamarre, F. Billard, C. H. Kerboua, M. Lequime, S. Roorda and L. Martinu, *Opt. Comm.*, 2008, **281**, 331–340.

13 C. Yu, X. Guo, M. Shen, B. Shen, M. Muzzio, Z. Yin, Q. Li, Z. Xi, J. Li, C. T. Seto and S. Sun, *Ang. Chem. Int. Ed.*, 2018, **57**, 451–455.

14 X. Wu, C. Hao, J. Kumar, H. Kuang, N. A. Kotov, L. M. Liz-Marzán and C. Xu, *Chem. Soc. Rev.*, 2018, **47**, 4677–4696.

15 H. Kang, F. m. c. A. Detcheverry, A. N. Mangham, M. P. Stoykovich, K. C. Daoulas, R. J. Hamers, M. Müller, J. J. de Pablo and P. F. Nealey, *Phys. Rev. Lett.*, 2008, **100**, 148303.

16 C. A. Mirkin, R. L. Letsinger, R. C. Mucic and J. J. Storhoff, *Nature*, 1996, **382**, 607–609.

17 R. Veneziano, S. Ratanalert, K. Zhang, F. Zhang, H. Yan, W. Chiu and M. Bathe, *Science*, 1986, **352**, aaf15.

18 M. Stevens, N. Flynn, C. Wang, D. Tirrell and R. Langer, *Adv. Mat.*, 2004, **16**, 915–918.

19 K. L. Gurunatha, A. C. Fournier, A. Urvoas, M. Valerio-Lepiniec, V. Marchi, P. Minard and E. Dujardin, *ACS Nano*, 2016, **10**, 3176–3185.

20 H. Tian and J. He, *Langmuir*, 2016, **32**, 12269–12282.

21 I. Koltover, J. O. Rädler and C. R. Safinya, *Phys. Rev. Lett.*, 1999, **82**, 1991–1994.

22 K. Sugikawa, T. Kadota, K. Yasuhara and A. Ikeda, *Ang. Chem. Int. Ed.*, 2016, 4059–4063.

23 M. Deserno and T. Bickel, *Europhys. Lett.*, 2003, **62**, 767.

24 E. J. Spangler, S. Upreti and M. Laradji, *J. Chem. Phys.*, 2016, **144**, 044901.

25 C. van der Wel, A. Vahid, A. Šarić, T. Idema, D. Heinrich and D. J. Kraft, *Sci. Rep.*, 2016, **6**, 32825.

26 R. Sarfati and E. R. Dufresne, *Phys. Rev. E*, 2016, **94**, 012604.

27 A. Šarić and A. Cacciuto, *Phys. Rev. Lett.*, 2012, **108**, 118101.

28 A. Šarić and A. Cacciuto, *Phys. Rev. Lett.*, 2012, **109**, 188101.

29 A. H. Bahrami and T. R. Weikl, *Nano Lett.*, 2018, **18**, 1259–1263.

30 E. J. Spangler, P. B. Sunil Kumar and M. Laradji, *Soft Matter*, 2018, **14**, 5019–5030.

31 Y. Zhu, A. Sharma, E. J. Spangler and M. Laradji, *Soft Matter*, 2022, **18**, 4689–4698.

32 E. Alizadeh-Haghighi, A. Karaei Shiraz and A. H. Bahrami, *Front. Phys.*, 2022, **10**,.

33 A. Sharma, Y. Zhu, E. J. Spangler, J.-M. Y. Carrillo and M. Laradji, *Soft Matter*, 2023, **19**, 1499–1512.

34 Y. Zhu, A. Sharma, E. J. Spangler, J.-M. Y. Carrillo, P. S. Kumar and M. Laradji, *Soft Matter*, 2023, **19**, 2204–2213.

35 A. Sharma, Y. Zhu, E. J. Spangler, T. B. Hoang and M. Laradji, *ACS Nano*, 2024, **18**, 12957–12969.

36 G. Karabiyik, A. Jesorka and I. Gözen, *Soft Matter*, 2024, **20**, 8947–8951.

37 J. Agudo-Canalejo and R. Lipowsky, *ACS Nano*, 2015, **9**, 3704–3720.

38 A. H. Bahrami, R. Lipowsky and T. R. Weikl, *Soft Matter*, 2016, **12**, 581–587.

39 Q. Yu, S. Othman, S. Dasgupta, T. Auth and G. Gompper, *Nanoscale*, 2018, **10**, 6445–6458.

40 M. Laradji, P. S. Kumar and E. J. Spangler, *Chem. Phys. Lipids*, 2020, **233**, 104989.

41 J. D. Revalee, M. Laradji and P. B. Sunil Kumar, *J. Chem. Phys.*, 2008, **128**, 035102.

42 M. Laradji, P. B. Sunil Kumar and E. J. Spangler, *J. Phys. D: Appl. Phys.*, 2016, **49**, 293001.

43 J. F. Nagle, M. S. Jablin, S. Tristram-Nagle and K. Akabori, *Chem. Phys. Lipids*, 2015, **185**, 3–10.

44 A. Sharma, Y. Zhu, E. J. Spangler and M. Laradji, *J. Chem. Phys.*, 2022, **156**, 234901.

45 Y. Zhu, A. Sharma, E. J. Spangler and M. Laradji, *Soft Matter*, 2023, **19**, 7591–7601.

46 J. R. Baumgardner and P. O. Frederickson, *SIAM J. Num. Anal.*, 1985, **22**, 1107–1115.

47 G. S. Grest and K. Kremer, *Phys. Rev. A*, 1986, **33**, 3628–3631.

48 A. Greiner, W. Strittmatter and J. Honerkamp, *J. Stat. Phys.*, 1988, **51**, 95–108.

49 B. Dünweg and W. Paul, *Int. J. Mod. Phys. C*, 1991, **02**, 817–827.

50 W. C. Swope, H. C. Andersen, P. H. Berens and K. R. Wilson, *J. Chem. Phys.*, 1982, **76**, 637–649.

51 H. X. Gan, H. Zhou, Q. Lin and Y. W. Tong, *Sci. Rep.*, 2017, **7**, 11565.

52 D. Boytsov, C. Hannesschlaeger, A. Horner, C. Siligan and P. Pohl, *Biotechnol. J.*, 2020, **15**, 1900450.

53 G. M. Torrie and J. P. Valleau, *Chem. Phys. Lett.*, 1974, **28**, 578–581.

54 S. Kumar, J. M. Rosenberg, D. Bouzida, R. H. Swendsen and P. A. Kollman, *J. Comp. Chem.*, 1992, **13**, 1011–1021.

55 V. T. Moy, E.-L. Florin and H. E. Gaub, *Science*, 1994, **266**, 257–259.

56 X. Chen, D. P. Tieleman and Q. Liang, *Nanoscale*, 2018, **10**, 2481–2491.

57 E. Atilgan and S. X. Sun, *J. Chem. Phys.*, 2007, **126**, 095102.

58 W. Helfrich, *Z. Naturforsch. C*, 1973, **28**, 693–703.

59 J. D. Revalee, M. Laradji and P. B. Sunil Kumar, *J. Chem. Phys.*, 2008, **128**, 035102.

60 T. Walz, B. L. Smith, P. Agre and A. Engel, *EMBO J.*, 1994, **13**, 2985–2993.

61 W. Humphrey, A. Dalke and K. Schulten, *J. Mol. Graph.*, 1996, **14**, 33–38.

Data for this article, including description of data types are available at Open Science Framework at https://osf.io/xp8tj. The molecular dynamics codes are available in GitHub at https://github.com/LaradjiSoftMatter/SoftMold.